





# HACS: Helical Auxetic Yarn Capacitive Strain Sensors with Sensitivity Beyond the Theoretical Limit

## Journal Article

### Author(s):

[Cuthbert, Tyler](#) ; [Hannigan, Brett C.](#) ; [Roberjot, Pierre](#) ; [Shokurov, Alexander V.](#); [Menon, Carlo](#) 

### Publication date:

2023-03-09

### Permanent link:

<https://doi.org/10.3929/ethz-b-000593970>

### Rights / license:

[Creative Commons Attribution-NonCommercial-NoDerivatives 4.0 International](#)

### Originally published in:

Advanced Materials 35(10), <https://doi.org/10.1002/adma.202209321>

# HACS: Helical Auxetic Yarn Capacitive Strain Sensors with Sensitivity Beyond the Theoretical Limit

Tyler J. Cuthbert,\* Brett C. Hannigan, Pierre Roberjot, Alexander V. Shokurov, and Carlo Menon\*

The development of flexible strain sensors over the past decade has focused on accessing high strain percentages and high sensitivity (i.e., gauge factors). Strain sensors that employ capacitance as the electrical signal to correlate to strain are typically restricted in sensitivity because of the Poisson effect. By employing auxetic structures, the limits of sensitivity for capacitive sensors have been exceeded, which has improved the competitiveness of this modality of sensing. In this work, the first employment of helical auxetic yarns as capacitive sensors is presented. It is found that the response of the helical auxetic yarn capacitive sensors (termed as HACS) is dependent on the two main fabrication variables—the ratio of diameters and the helical wrapping length. Depending on these variables, sensors that respond to strain with increasing or decreasing capacitance values can be obtained. A greater auxetic character results in larger sensitivities accessible at smaller strains—a characteristic that is not commonly found when accessing high gauge factors. In addition, the highest sensitivity for auxetic capacitive sensors reported thus far is obtained. A mechanism of sensor response that explains both the variable capacitance response and the high gauge factors obtained experimentally is proposed.

the population—health researchers to the general population—are able to better harness the data accessible from them. Application and translation of the fundamental improvements of sensors will enable improved diagnostics, monitoring, rehabilitation, and performance. Flexible and stretchable soft sensors in fiber forms are attractive for wearable device applications since they can be integrated directly as part of the textiles that make up our clothing and turn it into multifunctional devices, or be employed as tracking or monitoring sensors in exoskeletons or robotics.

Textiles make up the majority of what we wear on a daily basis. Integration of stretchable sensors is not a trivial pursuit because of the mismatch of mechanical properties between sensors and textiles; large differences in mechanical properties can cause issues with weaving or knitting and may cause irreversible damage to the sensors during fabrication. Reports of integration of sensors directly into tex-

## 1. Introduction

Wearable devices have been steadily increasing in popularity in both academic and commercial realms as a large portion of

tile have been reported, although they are typically limited to a single mechanism of sensing that has its limitations. Expansion of sensing technology that employs haberdasher-based solutions (i.e., yarn or thread) is still limited, and solutions that can provide alternative mechanisms of sensing will expand the potential of what wearable devices can accomplish.

Flexible fiber sensors typically come in three flavors—piezoresistive (the most prominent modality), inductive, and capacitive. The capacitive sensing mechanism has a distinct advantage in that it relies only on geometry; this feature eliminates any issues (signal inconsistency, drift, hysteresis, etc.) relating to the use of percolating conductive networks or rigid electrodes on flexible substrates employed in piezoresistive sensors. This distinct advantage over piezoresistive sensors is somewhat overshadowed by the dizzying number of reports quoting high sensitivity (i.e., gauge factor (GF)) at large strains (>100% strain, often over 1000%). Exceeding the current capabilities of these sensing modalities is crucial for advancing the technology, yet there are limited examples focusing on the development of sensitivity within the working strain range for applications such as textiles and wearable devices, which require sensitivity below 50% strain, and should possess mechanical properties in the range of textiles and skin ( $\approx 60$  KPa for textiles,<sup>[1]</sup>  $\approx 83.3 \pm 34.9$  MPa for skin<sup>[2]</sup>) that will aid in the translation of the technology to the market.

T. J. Cuthbert, B. C. Hannigan, P. Roberjot, A. V. Shokurov, C. Menon  
Biomedical and Mobile Health Technology Lab  
ETH Zürich  
Lengghalde 5, Zürich 8008, Switzerland  
E-mail: tyler.cuthbert@hest.ethz.ch; carlo.menon@hest.ethz.ch

P. Roberjot  
UFR Sciences and Properties of Matter  
University of Rennes 1  
Campus de Beaulieu, Rennes 35042, France

P. Roberjot  
Nanoscience, Nanomaterials, and Nanotechnology  
Adam Mickiewicz University  
ul. Wieniawskiego 1, Poznań 61-712, Poland

 The ORCID identification number(s) for the author(s) of this article can be found under <https://doi.org/10.1002/adma.202209321>.

© 2023 The Authors. Advanced Materials published by Wiley-VCH GmbH. This is an open access article under the terms of the Creative Commons Attribution-NonCommercial-NoDerivs License, which permits use and distribution in any medium, provided the original work is properly cited, the use is non-commercial and no modifications or adaptations are made.

DOI: 10.1002/adma.202209321

Increasing the sensitivity of capacitive strain sensors has thus far been limited since the electrical response of sensor is governed by the geometry of the capacitor and by the response of the materials that comprise it. Bulk materials conform to non-negative Poisson's ratio—a narrowing in the transverse axis to axial strain—which in turn, results in the limit of area expansion of the capacitors elements to a value smaller than the amount of strain applied. Capacitors fabricated with bulk polymer materials, then, cannot achieve sensitivities (i.e. GF) greater than one. Thus, to access higher sensitivities the common approach is to employ structures and designs that result in non-natural responses to strain (i.e., metamaterials or auxetic materials). Auxetic materials possess a negative Poisson's ratio<sup>[3]</sup> and have been employed in capacitive strain sensors most commonly in parallel plate configurations.<sup>[4–12]</sup> In these examples the authors were able to either expand the width of the parallel plate, or at least eliminate transverse narrowing upon an axial strain to achieve a larger increase in electrode area versus applied strain to result in delta capacitance changes that exceed GF's above the theoretical GF limit of one (Figure 1). Of the examples employing auxetic structures, GF's slightly above three have been achieved,<sup>[4,6]</sup> with most accessing GF's below two.<sup>[5,8,9]</sup> The application of auxetic structures are still in their infancy but have the potential to further increase the sensitivity of capacitive sensors, especially as sensors are downsized and take on structures/morphologies that are more amenable to integration into wearable devices, such as textiles.

Auxetic mechanical metamaterials have been categorized by Kolken et al. into re-entrant structures, chiral structures, and rotating semi-rigid structures, of which examples of each have achieved higher sensitivity in strain sensors non-specific to the sensing mechanisms (i.e., piezoresistive, capacitive, piezotransmittance, and so on).<sup>[3,10–12]</sup> Interestingly, auxetic structures employing yarns were first described by Hook et al. in 2006, which employ a rigid fiber helically wrapped around an elastic

core,<sup>[13,14]</sup> and have been studied experimentally and with some focused finite elemental analysis around their mechanical behavior. Thus far, only one example of employing auxetic yarns in strain sensing has been reported and the authors utilized a change in resistance—through a change in contact area—upon straining conductive fibers that were helically wrapped around an elastic fiber.<sup>[15]</sup> Thus far, there have yet to be helical auxetic yarns employed as capacitive sensors; likely this is because the impact of helical auxetic yarns (HAYs) behavior on capacitance is not as intuitive as a parallel plate configuration or with the resistance changes in previous works. With parallel plate configurations, the effect is straightforward with the focus on simply increasing the area of the electrodes of the capacitor more than the applied strain. HAYs on the other hand impact the total diameter of the 2-component fiber (Figure 1), and it is not immediately obvious if this response would have a positive effect on the GF of a sensor fabricated using this structure.

Herein, we report on the development of capacitive sensors that are in the form of helically wound yarns, experimental characterization of the sensors with respect to the two main variables in fabrication, and the development of a geometrical model that is then used to calculate capacitance and explain the electrical response. We first describe the helical auxetic yarn geometrical considerations to define the variables that define the fabrication parameters of the sensors. Then, fabrication of the sensors is described including the synthesis of an elastic and highly stretchable electrode by employing vapor polymerization of polypyrrole onto a polyester wound elastic fiber and the helical manufacturing by helical winding with a copper wire around the conductive elastic fiber. By varying the two dependent variables—the ratio of diameters between the fibers and the pitch of the helically wound fiber—we were able to vary the Poisson's ratio of the sensors to empirically determine the correlation of sensor sensitivity to auxeticity. Interestingly, we observed a range of responses from the HAY capacitive sensors (abbreviated as HACS), and propose a mechanism for the interesting response of the HACS, which possess the highest GF that has yet to be reported for auxetic capacitive sensors of any type.

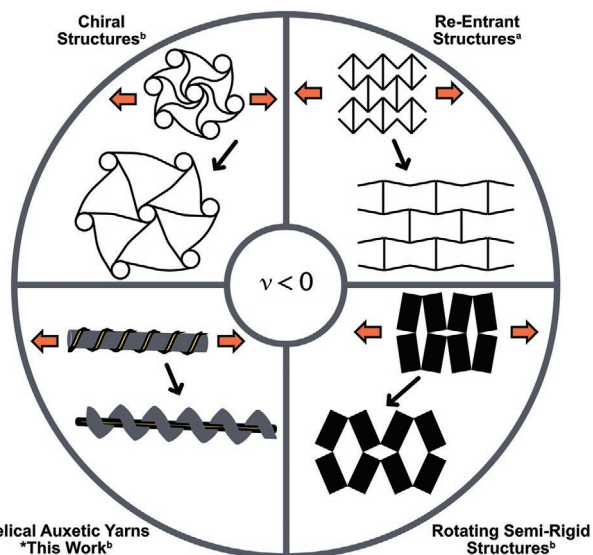


**Figure 1.** Representation of different auxetic mechanical structures currently known; this work will focus on utilizing helical auxetic yarns as sensors. Auxetic structures employed in capacitive sensors thus far (a) and auxetic structures not yet employed in capacitive strain sensors (b).

## 2. Results and Discussion

To begin, we sought to design a capacitive strain sensor that was capable of accessing greater sensitivity in a fiber form for direct integration into textiles. Theoretically, capacitive sensors are limited to a  $GF \leq 1$  with bulk materials since capacitance has a geometrical dependence (Equation (1)) and all bulk materials follow the Poisson's effect—a narrowing in the transverse axis to the applied strain—and therefore possess a Poisson's ratio ( $\nu \geq 0$ ).

$$\Delta C = \frac{\Delta A \epsilon}{\Delta d} \quad (1)$$

where  $\Delta C$  is the change in capacitance,  $\Delta A$  is the change in the area of the electrodes of the capacitor,  $\Delta d$  is the change in the distance separating the two electrodes, and  $\epsilon$  is the relative permittivity (i.e., dielectric constant) of the material separating the electrodes. Equation (1) indicates that only a change in the geometry of  $A$  or  $d$  would result in a capacitance change. The Poisson's ratio of natural materials in essence limits the

amount of area expansion of the electrodes and the thinning of the dielectric separator in response to strain ( $\epsilon$ ). Poisson ratio's of most solid materials lies between 0 and 0.5 and therefore upon straining the area increases at a rate below the value of  $\epsilon$ , which in turn results in a smaller  $\Delta C$  in comparison to  $\epsilon$  (Equation (2)) and therefore only produces GF's  $\leq 1$ :

$$GF = \frac{\frac{\Delta C}{C_0}}{\epsilon} \quad (2)$$

When fabricating a capacitive sensor in a fiber morphology—such as coaxial,<sup>[16–18]</sup> twisted fibers,<sup>[19]</sup> or sandwiched<sup>[20]</sup>—the method for calculating/modeling capacitance becomes more complex, but the Poisson effect still holds for all materials incorporated, even for the more exotic high-performance materials such as liquid metals or carbon nanotube forests. Therefore, any structure that employs materials that result in a “natural” response that follows Poisson's effect at the material and sensor level, will be limited in sensitivity/GF. Thus, we decided to look beyond what materials to employ and instead toward how to leverage the geometry that governs the capacitance by first attempting to understand and predict a general auxetic character under our desired sensor configuration. First, the HACS geometry will be described with respect to each of the capacitor elements and how this affects the resulting Poisson ratio of the sensor.

## 2.1. Simple Geometrical Description of the HACS

Generally, HAYs are systems composed of an inelastic flexible wire, ( $W_F$ ) of length  $L_W$ , diameter  $D_W$ , wrapped around

an elastic fiber ( $E_F$ ) of length  $L_E$ , diameter  $D_E$  with a specific pitch (as an angle,  $\theta$  for  $W_F$  and  $\phi$  for  $E_F$ , **Figure 2a–c**) or more intuitively a length associated with a complete helix (HL; helical length, **Figure 2d**).  $E_F$  also possesses an angle ( $\phi$ ), which is zero to begin with and increases as strain is applied.

HAYs evolve through three different states when undergoing strain. In the initial state, where no strain is applied to the sensor ( $\epsilon_i$ , **Figure 2**). When strain is applied, the  $W_F$  transitions from a helical to twisted to straight configuration and undergoes no elongation, whereas the  $E_F$  is elongated during strain—and therefore narrows simultaneously—and transitions from a straight to twisted to a helical state. For simplicity, we have instead identified these states as initial, twisted, and final (**Figure 2a**). For predicting the HACS behavior, we chose to focus on the initial and final state since this would allow us to complete an initial prediction of auxetic character at the easily defined initial and final states, which we could then use to compare to capacitance changes and GF's.

### 2.1.1. Parameters of the $W_F$

The final state, the  $W_F$  is straight ( $\phi_f = 0$ ) and  $E_F$  in a wrapped helical configuration around  $W_F$  ( $\phi_f$ , **Figure 2a**). The length of the sensor in the final state is the length of the  $W_F$  ( $L_W$ ), which can be obtained for each sensor by solving the right-hand triangle in **Figure 2b**. The maximum strain that can be applied to the sensor in the final state  $\epsilon_{\text{final}}$  is calculated with Equation (3):

$$\epsilon_{\text{final}} = \frac{L_W - L_E}{L_E} \quad (3)$$

We assume between the initial and final state the conservation of the number of helical turns ( $n$ ) per length of the sensor;

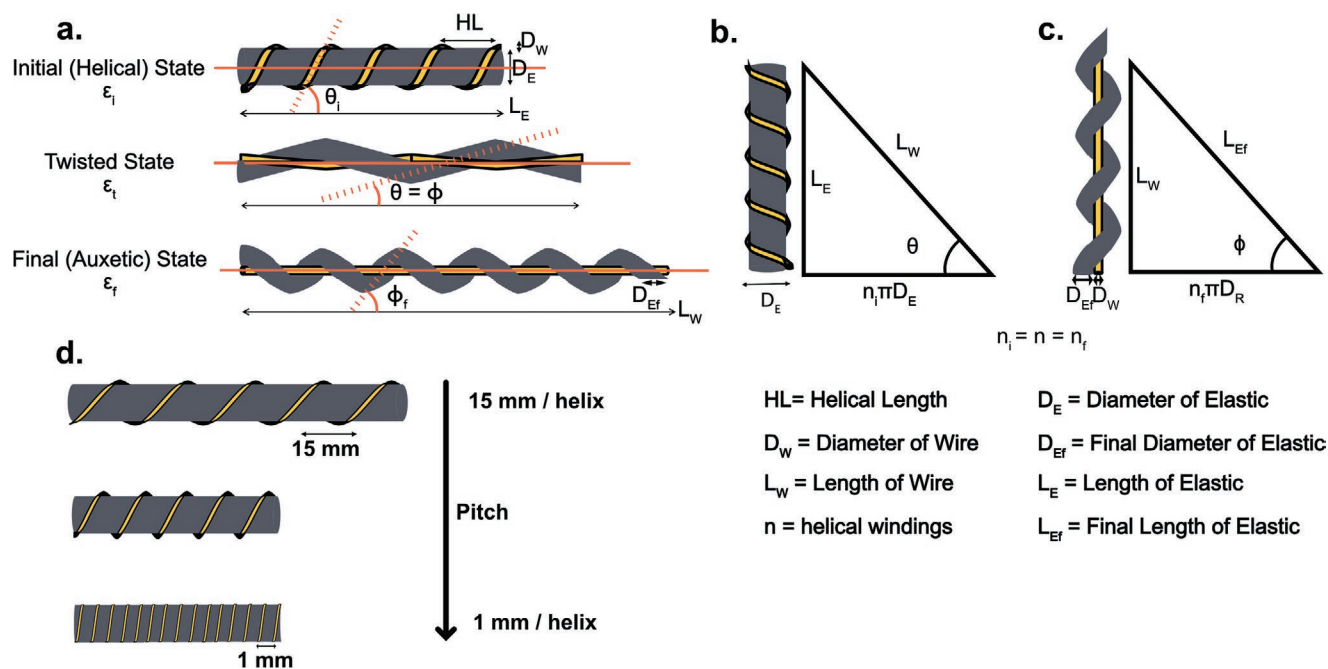


**Figure 2.** a) The representation of the three states of the sensor, the initial state, the twisted state, and the final state. b) Initial state geometrical representation; c) final state geometrical representation; and d) initial state of the HACS with different helical lengths tested in this report.

with this constant, we can easily isolate sections of the sensor based on the initial length of one helix of  $W_F$  around  $E_F$ , which we define as the initial HL, which can be converted to an angle with Figure 2 and Equation (4)

$$\theta_i = \tan\left(\frac{L_E}{n\pi D_E}\right) \quad (4)$$

The final angle of the  $W_F$  ( $\theta_f$ ) is, therefore, zero since it will be the inner fiber at the final maximum strained state ( $\epsilon_f$ , Figure 2). Since the  $W_F$  does not undergo tensile strain—rather it simply transitions from a helix to a straight fiber—it does not undergo any narrowing and the diameter of the  $W_F$  is constant.

### 2.1.2. Parameters of the Elastic Fiber

The  $E_F$  upon application of strain will begin to elastically elongate and transition to the twisted state to the final state, where it will be helically wound around  $W_F$  (Figure 2a). In similar fashion to determining the parameters of  $W_F$ , the important parameter we require to calculate Poisson's ratio of the HAY is only the final length and diameter of the  $E_F$  ( $L_{Ef}$  and  $D_{Ef}$ , respectively).

$L_{Ef}$  can be calculated through the right angle triangle (Figure 2c) and  $D_{Ef}$  can be approximated by assuming a relatively common elastomer Poisson's ratio of 0.4 for  $E_F$  using the following formula:

$$\Delta D_E = -D_{Ef} \left[ 1 - \left( 1 + \frac{(L_{Ef} - L_E)}{L_E} \right)^{-\nu} \right] \quad (5)$$

$\Delta D_E$  was calculated at  $\epsilon_f$  for a range of HACS at ratio of diameters of 10:1 and 20:1, assuming the number of helices is equal at the initial state and the final (and possibly auxetic) state (Table 1).

### 2.1.3. Poisson's Ratio of the HACS

Possessing the variables required to calculate the HACS, we employed Hencky's Poisson function (Equation (6)) to determine the auxeticity at  $\epsilon_f$ :

$$\nu_{\text{Hencky}} = -\frac{\ln\left(1 + \frac{\Delta D_{\text{HACS}}}{D_{\text{HACS}}}\right)}{\ln\left(1 + \frac{\Delta L_{\text{HACS}}}{L_{\text{HACS}}}\right)} = \nu_{\text{HACS}} \quad (6)$$

where we can find the term for the changing diameter of the HACS

$$\frac{\Delta D_{\text{HACS}}}{D_{\text{HACS}}} = \frac{(2D_{Ef} + D_{Rf}) - (2D_{Rf} - D_{Ef})}{\left(\frac{D_{Rf} - D_{Ef}}{D_{Ef}}\right)} \quad (7)$$

and the changing accessible strain of the HACS is simply a comparison of the initial length of  $E_F$  ( $L_E$ ) and the final length, which is the length of  $W_F$  ( $L_W$ ) (Equation (8)):

$$\frac{\Delta L_{\text{HACS}}}{L_{\text{HACS}}} = \frac{(L_W - L_E)}{L_E} = \epsilon_f \quad (8)$$

The results from this calculation can be found in Table 1 ( $\nu_{\text{calc}}$ ). We chose to study the resulting Poisson's ratio of HACS with two variables that we could easily change: i) the ratio of diameters of the  $E_F$  and  $W_F$  and ii) the initial HL; the chosen values were driven by the materials we intended to employ for these sensors (Table 1). The HACS we evaluated ranged from a diameter ratio between the  $E_F$  and the  $W_F$  of 20:1 (E3) and 10:1 (E1) with a range of starting HL's of  $W_F$  wrapped around  $E_F$  (Table 1). We determined we would access higher strain ranges as the HL is decreased but would also decrease the auxeticity. Increasing the ratio of diameters predicts access to higher auxetic character at a similar maximum strains (Table 1  $D_{Ef}/D_{Rf}$ , see Supporting Information for more information).

## 2.2. HACS Fabrication and Testing

With a simple model and prediction of the HACS parameters to obtain auxeticity at the sensors extremes, we focused on fabricating consistent and reliable stretchable conductive electrodes that were textile-based. The requirements for fabricating HAYS typically require a inelastic smaller diameter fiber and

**Table 1.** HAY capacitive sensor parameters and calculated values.

Sample <sup>a)</sup>	HL [mm helix <sup>-1</sup> ]	$D_E$	$D_W$	$D_E:D_W$	Max. strain <sup>b)</sup>	Auxetic	$\nu_{\text{calc}}^c$
E1W1-1	1	1.1	0.11	10:1	230%	N	0.33
E1W1-4	4	1.1	0.11	10:1	27%	Y	-1.8
E1W1-8	8	1.1	0.11	10:1	8%	Y	-7.41
E3W1-2	2	2.2	0.11	20:1	230%	N	-0.08
E3W1-4	4	2.2	0.11	20:1	86%	Y	-0.6
E3W1-8	8	2.2	0.11	20:1	27%	Y	-2.2
E3W1-15	15	2.2	0.11	20:1	9%	Y	-10.7
E3W1-3	3	2.2	0.11	20:1	119%	N	-0.4

<sup>a)</sup>E = Elastic; W = wire; numbers following the letter equate to the number employed; <sup>b)</sup>calculated; <sup>c)</sup>calculated at max strain.

a larger diameter elastic core ( $W_F$  and  $E_F$  in our calculations, respectively). In addition, an insulating material would be required between the electrodes to obtain capacitance. High gauge (0.11 mm diameter,  $\approx 41$  gauge) enamel coated copper wire was used as the  $W_F$  electrode because it is highly flexible but non-extending under the expected forces; it also possesses a highly consistent and thin insulating layer that is ideal for this application. To obtain a conductive  $E_F$  we employed a scalable and sustainable vapor phase polymerization of conductive polymer—polypyrrole—on a polyester wrapped elastic fiber (analogously termed  $E_F$ ) to fabricate the elastic fiber electrode ( $PPy-E_F$ , Figure 3a). By first soaking the  $E_F$  in a 3 M methanol solution of  $FeCl_3$ , drying, and then exposing to pyrrole vapors we were able to obtain uniform deposition of polypyrrole on and within the multifilament polyester fiber sheath (Figure 3a, more scanning electron images can be found in the Supporting Information). The resulting  $PPy-E_F$  possessed conductivity suitable for fabricating capacitors with resistance in the range of  $10 \text{ k}\Omega \text{ cm}^{-1}$  with minimal piezoresistance (see Supporting Information for details, and Video S1, which shows the process of polymerization).

With the components of the capacitor in hand, we fabricated the HACS' with various HL's. The HACS' were characterized using a linear strain to break (or 100%, whichever occurred first) to determine the typical response throughout the accessible strain range (see Supporting Information). When the HACS were strained beyond their maximum strain range, they would either break or the signal slope would decrease and flatten as a result of slippage of the  $W_F$  wire against the much larger  $PPy-E_F$ . Therefore, we used this information to determine the working region of our HACS, which were experimentally close

to the expected maximum strain determined in Section 2.1. With freshly fabricated HACS and an understanding of how the sensors were responding we moved on to analyzing the GF's and hysteresis of each sensor. The HACS were strained with an increasing triangular strain pattern at 10% increments to either the maximum strain or 40% strain (typical strain observed in athletic clothing, Figure 4a,b).

### 2.2.1. E1W1 HACS Hysteresis and Gauge Factor

First, HACS comprised of one  $PPy-E_F$  and one  $W_F$  (E1W1-8/-4/-1) with a range of HL's and a ratio of diameter of 10:1 were characterized and resulted in very different, and unexpected capacitive response to strain. E1W1-8 was essentially unusable as a sensor and could only access a few percent strain; while it showed a high potential GF with a steep slope, it was eliminated from further analysis as it almost immediately sustained irreversible damage. It is worthy to note that this sensor was predicted to have a large negative Poisson's ratio and it almost immediately completed the HAY "flip" upon the application of strain (i.e., the transition from the twisted to the final state). E1W1-4 had an accessible strain range of close to 30% strain and possessed a linear capacitance response to strain with a GF of 0.85 and was auxetic completing the HAY "flip" as predicted (Figure 4c). E1W1-1—the HACS with the tightest helical winding (i.e., lowest HL), and preserved the initial  $W_F$  helical winding throughout our testing range not accessing the twisted state (Figure 4e). E1W1-1 did not complete the HAY "flip" within our testing range of 40% strain (or even within the accessible limit of  $E_F$  of 100% strain).

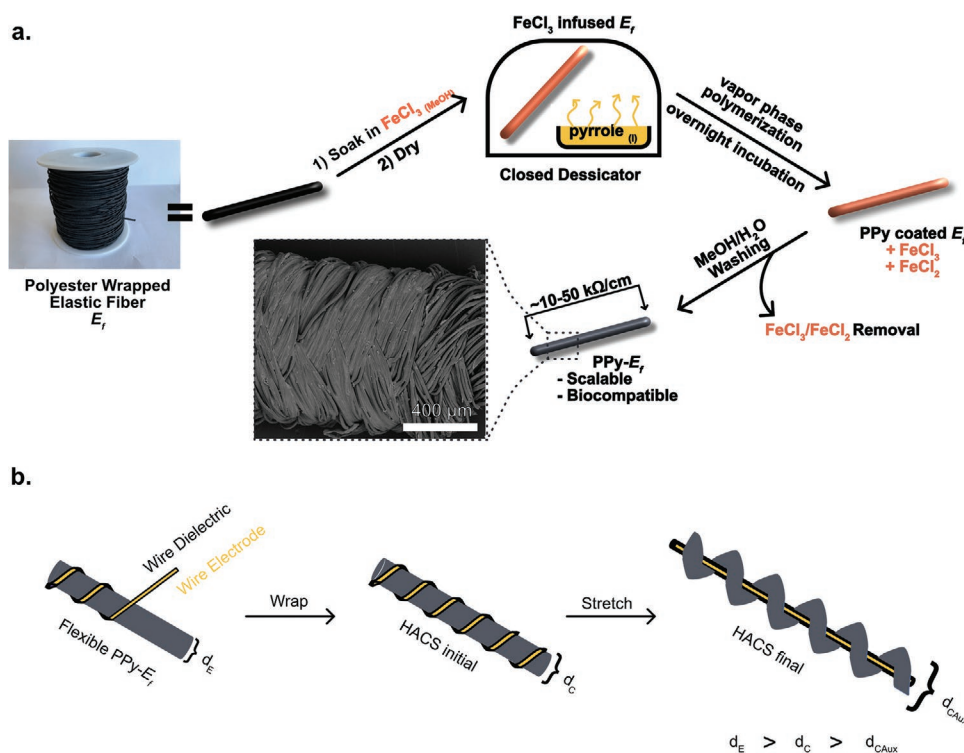


**Figure 3.** a) Fabrication of  $PPy-E_F$  including SEM-BSED image. b) Manufacturing of the  $F_C$  by wrapping the  $W_F$  helically around the  $E_F$ .

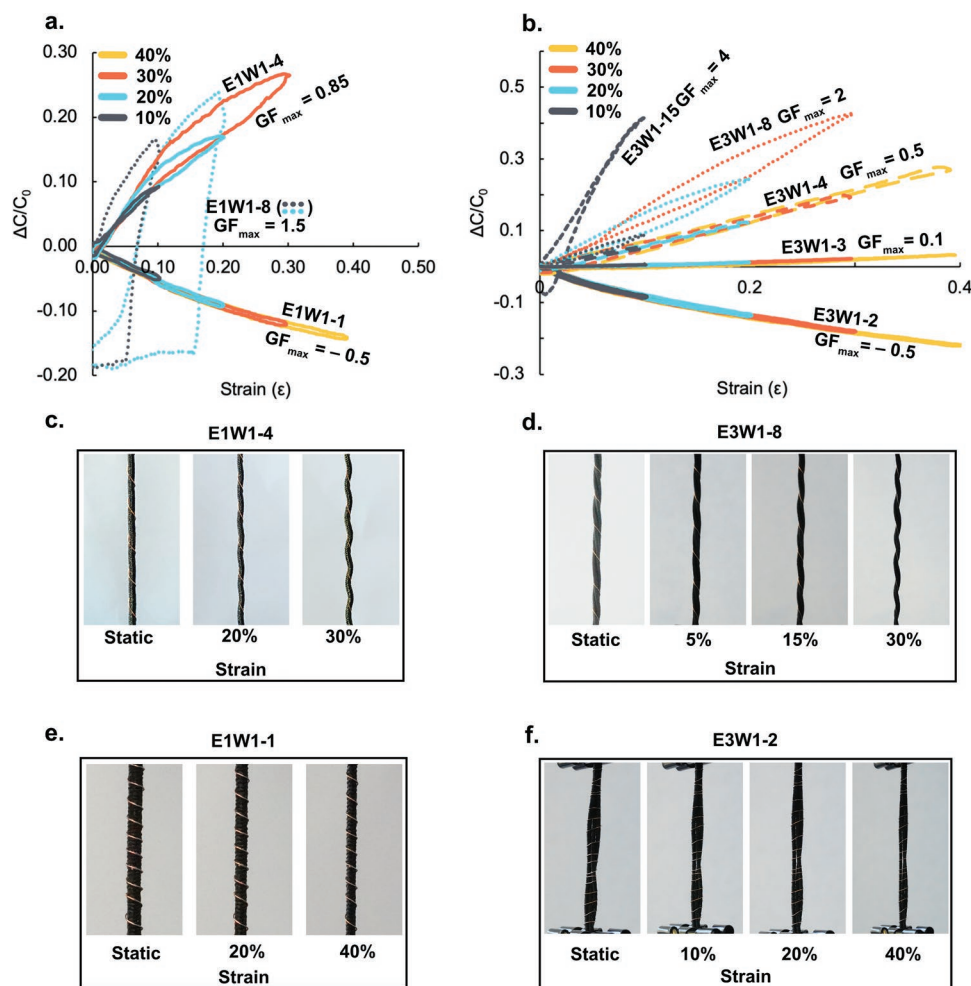


**Figure 4.** Strain–delta capacitance hysteresis plots for HACS. a) E1W1 and b) E3W1. c–f) Images of non-auxetic and auxetic HACS at the initial, twisted, and final states.

### 2.2.2. E3W1 HACS Hysteresis and Gauge Factor

To analyze the effect of employing a larger ratio of diameters of 20:1 three  $PP\gamma-E_F$  electrodes were then wound with one  $W_F$  at different HL's (see Table 1). Employing the similar HL's as above, it is intuitive that a larger ratio of diameters would result in a greater maximum strain for analogous HL values because of the larger circumference each helix is required to complete. Similarly to E1W1-1, we calculated that E3W1-2 would possess a positive Poisson's ratio, which experimentally we confirmed (Figure 4f). E3W1-2 was not auxetic (i.e., it did not complete the HAY “flip”) up to the 100% strain limit of  $PP\gamma-E_F$ , although it was predicted to be auxetic at its final state this was not attainable with the limits of strain  $E_F$  could undergo (Table 1). E3W1-2 also possessed a negative change in capacitance upon strain similarly to E1W1-1 (Figure 4b). E3W1-4 was calculated to possess a negative Poisson's ratio (Table 1), but did not possess a GF greater than one. Increasing the HL to 8 mm (E3W1-8) resulted in an increase in GF beyond the theoretical limit to a value of two, which coincided with an increase in auxetic character. Increasing the HL further to 15 mm (E3W1-15) resulted in the largest GF that we obtained that was able to repetitively

strain to at 10% and possessed a GF of four (Figure 4b, see Supporting Information). It was obvious that an increase in auxetic character (i.e., the more negative the Poisson's ratio) resulted in an increase in GF in the positive direction.

### 2.2.3. Poisson's Ratio Correlation to Capacitance Change

The different directions of positive (E1W1-1 and E3W1-2) or negative (all other sensors) capacitance change in response to strain—at least within our testing region—that we observed intrigued us to further investigate and explain why this phenomenon was occurring. We hypothesized that if this correlation of auxeticity to GF were to hold true, a HACS that possessed a Poisson's ratio exactly—or as close as possible—to zero would result in no capacitance change upon the application of strain. Since E3W1-2 and E3W1-4 were essentially equal GF's with opposite signs, we proposed that a HACS with a HL of three would result in a sensor that would not respond to strain. E3W1-3 was fabricated and the strain to capacitance relationship was characterized. E3W1-3 had as close to a zero GF as we could produce (GF = 0.1), although it was calculated to have

a slightly negative Poisson's ratio at its maximum strain. Our simple method of comparing the initial and final HACS diameters to determine Poisson's ratio seemed to work for predicting the trend, but could not explain why we were obtaining negative capacitance changes; for this, we looked closer at how the HACS were evolving during strain and how this would affect the resulting capacitance between the two electrodes.

#### 2.2.4. Calculation of Capacitance and Prediction of Gauge Factors

Previously, capacitive sensors that employ twisted fibers, and hollow double helical fibers have had capacitance prediction successfully modeled by employing the capacitance calculated from two parallel wires.<sup>[4,19]</sup> We completed a similar analytical prediction of our HACS, which required a slightly more complex model since our electrodes are different dimensions and change differently upon the application of strain. We employed a more advanced geometrical model (extensive details provided in the Supporting Information) that was able to calculate the cross-sectional maps of the elements of the HACS at any given strain percent with the desired starting configurations along with the ability to vary the Poisson's ratio for the  $E_F$ . This model provided an additional visual tool to observe the progression of the various HACS in 3D, create cross-sectional maps to integrate geometrical changes of our elements at any given strain to calculate capacitance, and most importantly GF's for any given initial parameters. We calculated capacitance using a transmission line capacitance calculator (essentially a more accurate version of the simple parallel wire calculation, ATLC2<sup>[21]</sup>).

The classical calculation for the capacitance of two parallel wires assumes: i) that the wires are composed of inelastic materials and ii) in the case of the two wires where one is helically wrapped around the other, there is a single contact path between the two elements. By employing an inelastic flexible fiber and an elastic fiber together, there will be mechanical effects that may not agree with assumption (ii) above. In addition, if  $W_F$  is a significantly higher modulus than  $PP\gamma-E_F$ , then  $W_F$  in the absence of  $PP\gamma-E_F$  is essentially a spring and by itself will have its own specific Poisson's ratio (of the helix), which may be different than the Poisson's ratio of  $PP\gamma-E_F$  within the helix. We first considered how the GF obtained by E3W1-15 and E3W1-8 was possible from a parallel wire capacitance calculation—both above a GF of 1 and both with a large auxetic character. The auxetic character can be thought of as the difference between the Poisson ratios of the  $PP\gamma-E_F$  and the  $W_F$  helical coil. If the  $W_F$  helical coil narrows at a rate faster than the narrowing of the  $PP\gamma-E_F$ , then there will be auxetic character; the greater the Poisson's ratio of the  $W_F$  helical coil—which equates to a larger HL—the more force that the  $W_F$  will apply to the  $PP\gamma-E_F$  as it moves  $E_F$  out of the way as it narrows until it is in its linearly straight final state (see visualizations in Videos S2 and S3, Supporting Information). With our advanced geometrical model, we still had to limit the elements (i.e.,  $E_F$  and  $W_F$ ) interaction such that at point that they would be rigid cylindrical contact surfaces and undergo no deformation in response to forces against each other; considering this scenario, we were still not able to calculate GF's greater than one for even highly auxetic sensors. We hypothesized that then, the only factor we were not

accounting for in our model was the difference in mechanical properties between the  $E_F$  and  $W_F$ , so to explain the HACS that possessed GF's above one, we proposed that the force of  $W_F$  against  $PP\gamma-E_F$  upon straining induces an engulfment of the  $W_F$  into the  $PP\gamma-E_F$  electrode; this comparison between point contact and engulfment is depicted in Figure 5b where we calculated the final geometry and forced the  $W_F$  electrode into engulfment of  $E_F$  at different percentages. Engulfment refers to  $W_F$  pushing into  $E_F$ , such that there is an increase in the contact area between the two fibers. For calculations of GF versus engulfment, we manually shift the position of the cross-section of the wires radially toward the center of the  $E_F$  by a fraction of its diameter.

As examples, we calculated what the GF's would be for our HACS E3W1-15 and E3W1-8 at various engulfment percentages (Figure 5c) and highlighted the engulfment percent that would match with our empirical findings (Figure 5c). E3W1-15 was proposed to have an engulfment of  $\approx 7\%$  and E3W1-8 an engulfment of  $\approx 12\%$ . For HACS that complete the helical "flip", we hypothesize that the relationship to GF is related to the mechanical properties of the  $E_F$  under different axial stresses. With higher strain (and therefore stress), the force to impart cross-sectional deformation (i.e., transverse strain) also increases. Deformation in the cross-section of the  $E_F$  is then easier at lower strains such as in our sensor E3W1-15 in comparison to E3R1-8.

Alternatively, E1W1-1 and E3W1-2 possessed negative GF's and positive Poisson ratios within our testing strain range; both possess a low HL resulting in a tighter helical wind of  $W_F$  around  $PP\gamma-E_F$ . A lower HL intuitively results in a lower Poisson ratio for the  $W_F$  since the narrowing of the helix occurs over a longer strain range since a lower HL over the same sensor length increases the length of the  $W_F$ . If the Poisson ratio of the  $W_F$  helix is less than the Poisson ratio of the  $PP\gamma-E_F$ , then upon strain there will be a gap formed between the  $W_F$  and the  $PP\gamma-E_F$ , which would result in a reduction of capacitance in response to the distance between the electrodes increasing (see animation in Video S4, Supporting Information). With the starting parameters of the sensor E3W1-2, we changed the  $E_F$  Poisson ratio and were able to obtain the observed decreasing capacitance upon strain. In some instances, such as our non-sensing HACS E3R1-3, it is then likely that these two effects are essentially offsetting and the Poisson ratios of the  $W_F$  helix and the  $E_F$  are equal (Video S5, Supporting Information). Until this point, we have assumed that the combination of  $E_F$  as the inner electrodes will respond as a single core inner electrode. To ensure that our results were not because of the non-smooth nature of the multifilament  $PP\gamma-E_F$  core of the inner electrodes, we analyzed a HACS fabricated from a smooth conductive rubber  $E_F$ , and obtained analogous results (see Supporting Information). The hand fabrication process introduced some variability in the sensors performance (Figure 5e) but was consistently able to produce both negative and high GF HACS.

To confirm the proposed mechanism, we employed light microscopy, electron microscopy, and X-ray microcomputed tomography ( $\mu$ CT) to visualize the interaction of the  $W_F$  and  $E_F$ ; we completed analysis on HACS fabricated with the  $PP\gamma-E_F$  (see Supporting Information) and a monofilament rubber  $E_F$  (Figure 6) to reduce the complexity of analysis and



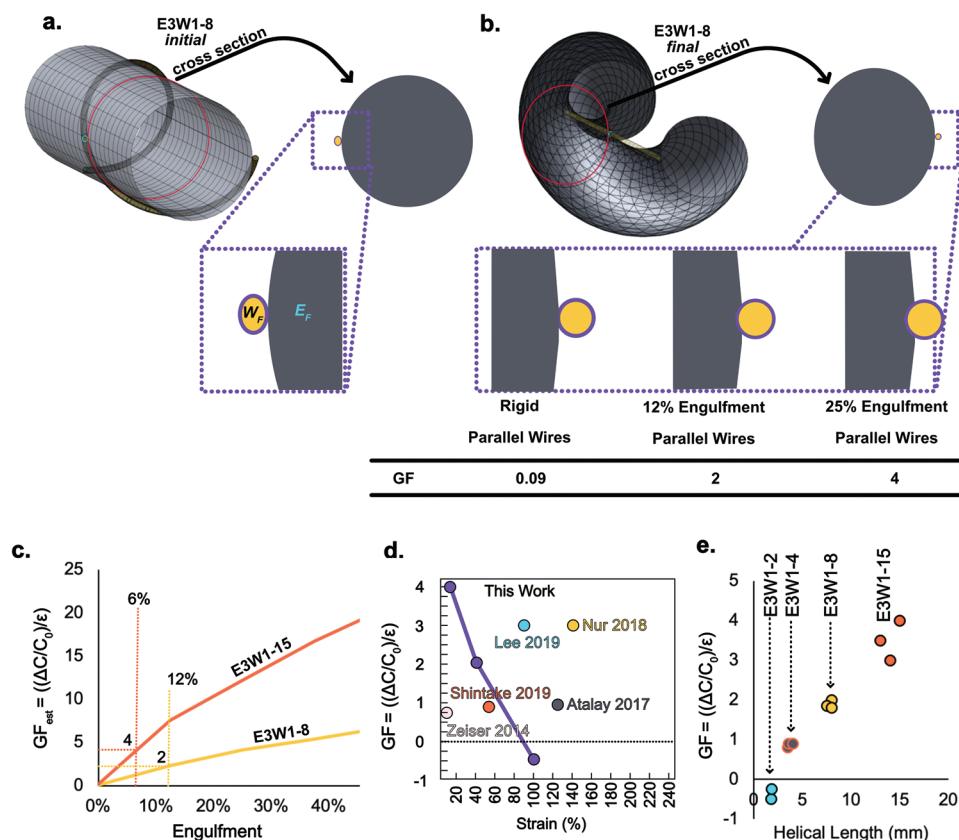


**Figure 5.** a,b) 3D representation of the HACS in the initial (a) and final (b) states and the 2D cross-sectional parallel wire morphology associated with point contact and engulfment examples. c) The GF calculated as a percentage of engulfment and the corresponding percentages that would match the empirical results. d) A map of the current highest performing auxetic capacitive strain sensors. e) GF obtained from various E3W1 HACS with different HL's.

provide better visualization. We overlaid our model on the  $\mu$ CT image for approximate parameters of the sensors analyzed. Three samples were analyzed: an unstrained HACS (equivalent to E3W1-4, Figure 6a, middle), a low HL HACS ( $\approx$ equivalent to E3W1-2) strained to 50% (Figure 6a, left), and a high HL HACS ( $\approx$ equivalent to E3W1-8) strained to 25% (Figure 6a, right). The  $\mu$ CT was ideal since the  $W_F$  and  $E_F$  are easily distinguished and allowed a non-destructive analysis of the HACS in strained states using a 3D printed fixture (see Supporting Information). As proposed, the HACS with a low HL upon straining produced a gap between the  $W_F$  and  $E_F$  (Figure 6b, left), which we also observed with a light microscope (Figure 6c, left). The unstrained HACS showed a surface contact point as expected (Figure 6b,c, middle). In the images from high HL HACS—possessing auxetic character—the  $W_F$  was observed to be mechanically deforming the  $E_F$  in the SEM images, which was in agreement with the  $\mu$ CT imaging where we observed  $\approx$ 30% engulfment of the  $W_F$  into the  $E_F$  (Figure 6b,c, right). These data are a direct confirmation of the engulfment hypothesis. While the degree of engulfment observed in the  $\mu$ CT differs from the expected value, the presence of engulfment evidently affects the geometry of the sensor. Future work will focus on how the material properties of  $W_F$  and  $E_F$  impact the engulfment phenomenon and sensor sensitivity.

These data represent HACS that span a wide range of accessible strains, electrical responses, and sensitivities. In comparison to other auxetic capacitive sensors, we have accessed the highest GF's thus far. While works such as Nur et al., Atalay et al., and Lee et al. were able to access high strain percentages with the parallel plate morphology, a large variety of sensor applications require high sensitivities at lower strains, such as textile-based wearable devices or exoskeletons, which this technology provides access to refs. [4, 6, 9]. At low strain percentages, Zeiser et al. and Shintake et al. have produced auxetic capacitive sensors that have exceeded the theoretical GF limit of one, which we have improved upon to increase that accessible sensitivity to GF's of four.<sup>[5,8]</sup> The textile form of the HACS is advantageous for seamless integration into textiles for clothing or wearable devices but may also find use in other applications such as robotics that can take advantage of the small volume and flexible nature of the fiber sensor.

### 2.2.5. HACS Additional Figures-Of-Merit

Wearable strain sensor performance—beyond GF—is commonly characterized by the response to increasing frequencies, the sensor's stability, and the response to changes in temperature; these figures-of-merit represent variables that

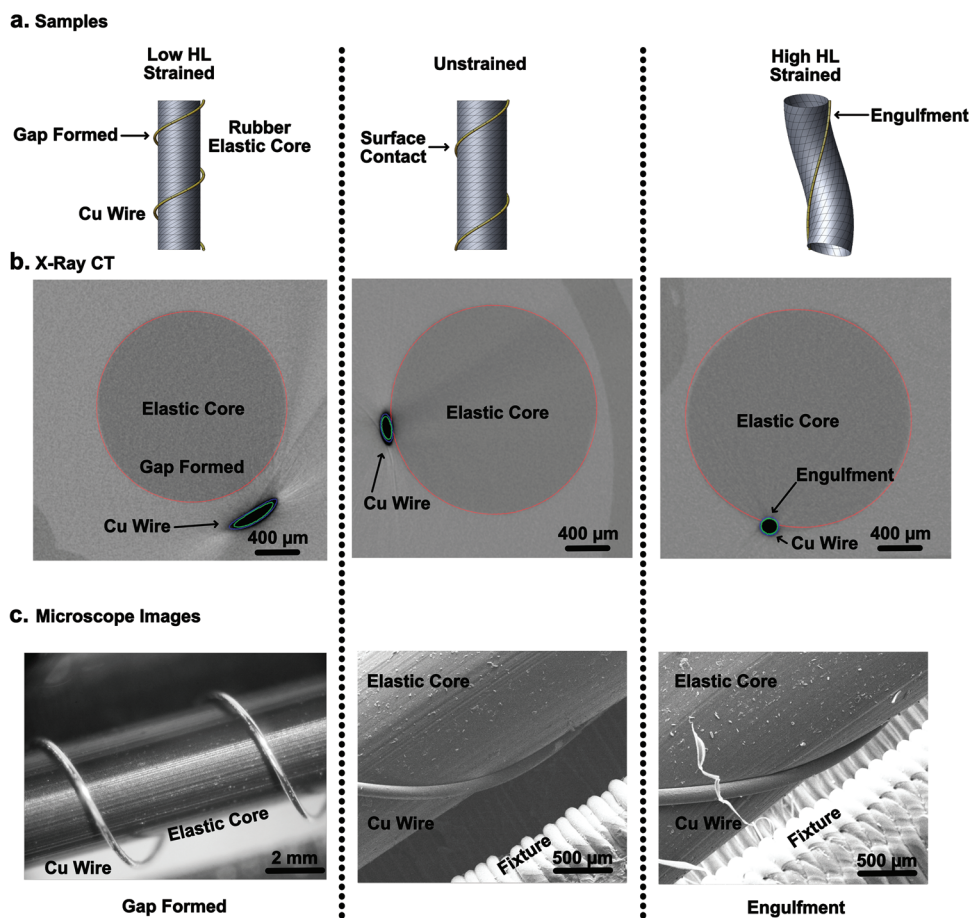


**Figure 6.** a) Samples representing strained and unstrained HACS depicting the gap formation and engulfment mechanism. b) X-ray microcomputed tomography ( $\mu\text{CT}$ ) of the samples described in (a) overlaid with our HACS model for the specific sample, RAW  $\mu\text{CT}$  images can be found in the Supporting Information. c) Light and scanning electron microscopy images of samples from (a) showing the gap and engulfment phenomenon in comparison to an unstrained HACS (middle).

wearable sensors may encounter when employed. The HACS' were tested for response to increasing frequency by straining in a sinusoidal strain pattern from 10–30% strain—a range that textile wearable sensors may regularly encounter. The human body moves at fairly slow frequencies below 10 Hz, with a sprinter achieving the highest frequencies of major limbs up to 8 Hz; certain non-conscious movements such as seizures can be greater than 10 Hz. Therefore, the HACS' capacitance response was analyzed from 1 to 20 Hz (Figure 7).

The frequency responses from two sensors are compared to highlight the difference between a sensor with a high GF that is nearing its maximum strain (E3W1-8) versus a non-auxetic sensor (E1W1-1) with a lower GF and well within its maximum strain. It was observed that both E1W1-1 and E3W1-8 responded well at low frequencies at, and below 5 Hz; both sensors at 1 Hz possessed accurate tracking over 50 cycles with E3W1-8 showing some minor variations in peak and troughs of the sine wave. At a frequency of 10 Hz, E3W1-8's response was severely modulated, which would not be suitable for monitoring tremors or seizures; E1W1-1 on the other hand was still able to track the sine wave at 10 Hz with some variations in peak and troughs. At 20 Hz, severe modulation was present in both E3W1-8 and E1W1-1, although E1W1-1 was still able to track the 50 peaks

and troughs (see Supporting Information). These data indicate that E1W1-1 could be employed to monitor high-frequency movement detection up to at least 20 Hz, while accurate strain tracking would be sufficiently accurate below 10 Hz for motion tracking applications. The greater auxetic character of E3W1-8 does provide the required performance for use in wearable devices tracking motion but does limit the applicability in high-frequency strain tracking, although this may be improved by employing  $E_F$  materials with improved resilience.

To analyze the long-term consistency of the HACS, we completed 1000 cycles of a sinusoidal wave pattern between 10–30% strain—a typical working range of a textile/clothing strain sensor—with E1W1-1 and E3W1-8 again to highlight the differences between the sensors (Figure 8a). E3W1-8 showed a minor increase in peak and trough heights within the first 50 cycles, after which it stabilized; E1W1-1 showed a highly stable signal with no indication of any change in peak or trough height, highlighting the advantages of utilizing a sensor well below its maximum accessible strain. The average capacitance of E3W1-8 between the initial 50 cycles versus the final 50 cycles was 1.4%, whereas E1W1-1 had a difference of only 0.2%. The high stability of the HACS highlights the advantage of the capacitive sensor design and the employment of elastic

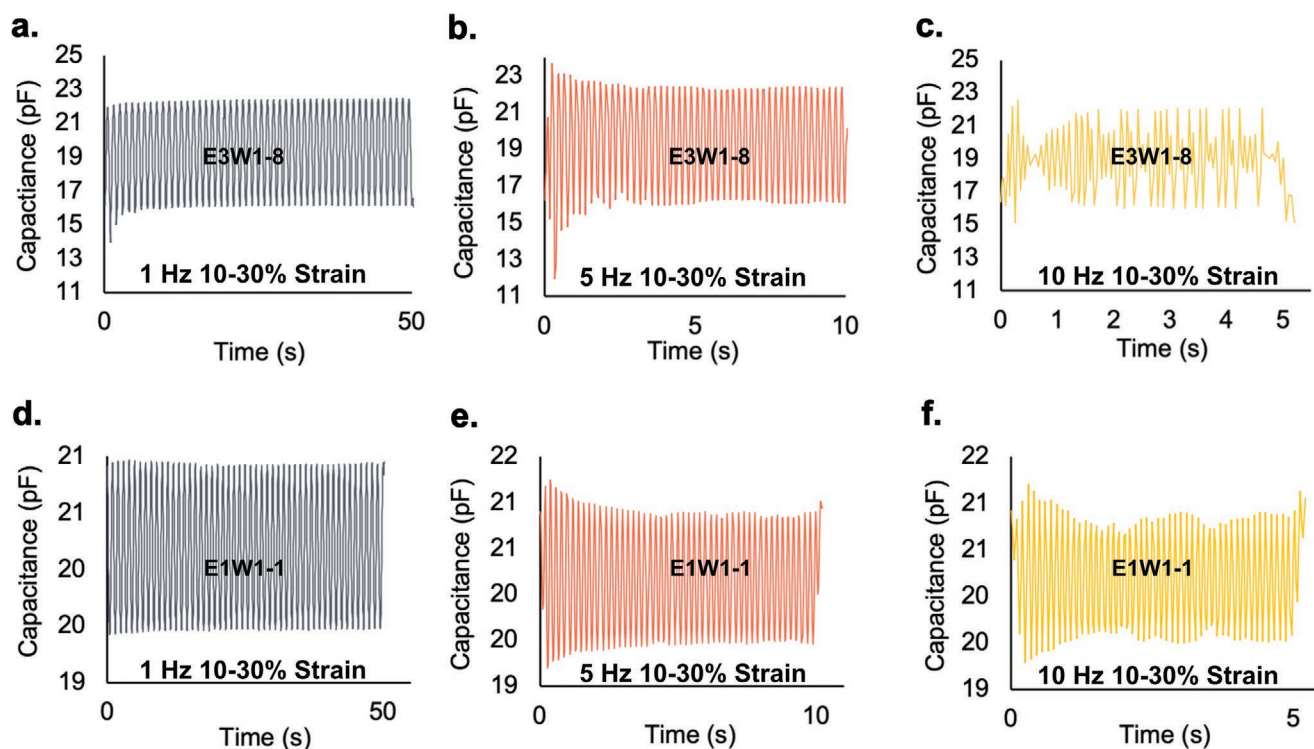


**Figure 7.** Frequency response of E3W1-8 and E1W1-1 at 1, 5, and 10 Hz (or 20 Hz, see Supporting Information).

materials well within their elastic regime. Both the material properties and the capacitance of sensors produced with polymeric materials are dependent on temperature—a variable that is highly likely to be changing within day-to-day use. Therefore, E1W1-1 baseline capacitance was compared between 4 and 40 °C and showed a negligible difference in baseline capacitance when within this temperature window (Figure 8c).

Lastly, since these sensors are helically wound, they respond to torsional strain. A variety of E3W1 HACS were twisted in 360° increments up to 1080° in the helical direction effectively increasing the number of helices, which resulted in an increase in capacitance, including under strain. While we have outlined primarily tensile strain in this report, the torsional sensing capabilities of the HACS may be advantageous in certain applications (Figure 8d).

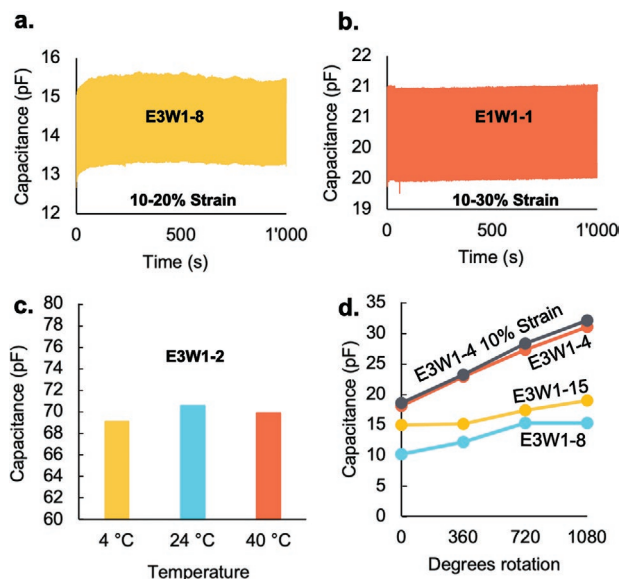


**Figure 8.** a,b) 1000 cycles stability for E3W1-8 (a) and E1W1-1 (b). c) Temperature dependence of the base capacitance of E1W1-1. d) Effect of twisting on E3W1 HACS capacitance.

### 3. Conclusions

We have employed helical auxetic yarn structures as capacitive strain sensors and uncovered unexpected responses from different sensor configurations. We utilized analytical models to describe the HAYS expected Poisson ratios using only pitch and the ratio of diameters as variables, which guided our fabrication of the sensors. We fabricated a range of HACS to experimentally determine if auxetic character correlates to GF and found that it not only affects GF, but the sign of capacitance change upon strain, which can be both positive or negative depending on the pitch of the helical windings of the initial outer helical element. We were able to obtain GF's as high as four at low strain percents, which are underrepresented in the area of strain sensors. We employed a scalable and sustainable vapor phase polymerization of conductive polypyrrole to produce the elastic inner fiber electrodes. The sensors were modeled to determine the geometry at any given strain, which allowed us to gain insight into how the Poisson ratio's of both the helix and the inner elastic fiber may affect the resulting capacitance changes upon undergoing strain. We proposed a

mechanism that was able to explain the capacitance changes of all of our sensors, where we see an increase in the sensitivity of the highly auxetic sensors as a result of electrode engulfment, which is the relationship of the relative ratios of the Poisson ratios of the capacitor elements and the moduli of the materials. The negative change in capacitance was reasoned to be caused by a mismatch of Poisson ratios of the helix and the inner elastic fiber, where the inner elastic fiber narrows at a rate faster than the helical coil causing a separation of electrodes upon strain—the opposite effect to the high GF sensors. Our HACS are relatively easy to fabricate, including the versatility of the vapor-phase electrode synthesis, and can be employed as standalone sensors or integrated into textiles, wearable devices, exoskeletons, or other mechanical devices with relative ease because of the soft and flexible nature of the yarn structure.

## 4. Experimental Section

**General Experimental:** All reagents were purchased from Sigma Aldrich and used as received unless otherwise stated. Pyrrole was purified by running an alumina plug (see Supporting Information for details). The base elastic fiber (800  $\mu\text{m}$  diameter; PET wound elastomer/rubber) was purchased from Spitzentrum (Zurich, Switzerland) and used as received. The copper wires with enamel coatings used as electrodes were purchased from Digitec-Galaxus (110  $\mu\text{m}$  diameter; Switzerland). Inductance–capacitance–resistance (LCR) measurements were made with a Hioki IM 3536 (purchased from Linktronix; Switzerland). The tensile testing was completed on an Instron ElectroPulse E3000. Calculations for modeling the capacitance were completed using the software Maple. Scanning electron microscopy was completed on a Quanta 200F FEI and sputter coated with 8 nm of Pt/Pd for imaging. Strained samples were imaged using a custom 3D printed fixture (see Supporting Information for details).  $\mu\text{CT}$  imaging was completed on a Scanco  $\mu\text{CT}$  45 Scanner at 90 kVp with an 8 mm diameter sample holder and the custom 3D printed fixture.

**Stretchable Fiber Electrode Fabrication:** The inner elastic polypyrrole fiber electrodes ( $\text{PPy}-E_f$ ) were fabricated by first soaking a length of elastic fiber ( $E_f$ ) in a solution of  $\text{FeCl}_3$  in methanol (3 M) for 15 min and then air dried. The  $\text{FeCl}_3$  impregnated  $E_f$  was then inserted into a glass desiccator with an open volume of pyrrole (1 mL). The vapor polymerization was allowed to proceed for 15 min, at which time it was removed and repetitively stretched to the fiber's maximum strain ( $\approx 100\%$ ). The  $E_f$  was then inserted back into the closed desiccator with the open volume of pyrrole and allowed to continue vapor phase polymerization; this removal–stretch–re-insertion was completed a total of four times. The vapor phase polymerization was then allowed to proceed overnight. The  $E_f$  was then removed and the residual  $\text{FeCl}_3$  was then removed from the  $\text{PPy}-E_f$  by soaking the fiber in methanol and water. The conductive  $\text{PPy}-E_f$  fibers were then air dried and kept in a sealed bag until use.

**Fabrication of the Sensors:** The auxetic capacitive sensors were fabricated by tying an overhand knot at each end of the  $\text{PPy}-E_f$  (1 or 3  $\text{PPy}-E_f$ ). The copper wire was then manually wound around the  $\text{PPy}-E_f$  ensuring that the wire had a consistent pitch and then secured on the outer end of each  $\text{PPy}-E_f$  knot with three half hitches. On one end of the excess copper wire, the enamel was removed using 150 grit sandpaper where the alligator clip of the LCR was attached, with the other alligator clip attached to the  $\text{PPy}-E_f$ .

**Tensile Testing and Capacitance Measurements:** The helical auxetic capacitive sensors (HACS) were tested on a tensile tester (Instron E3000) and custom design 3D printed grippers (see Supporting Information for images). An LCR was used to monitor the sensor's output by attaching

one lead to the exposed copper wire and the other to a free end of the  $\text{PPy}-E_f$  electrode. Series capacitance, series resistance, phase angle, and impedance were measured during all tensile testing at a sampling frequency of 1 kHz and at a strain rate of  $1\text{mm s}^{-1}$ .

**Gauge Factor Calculation:** The resulting signal files from the tensile tester and LCR device were resampled to 100 Hz. This resample was completed to allow the comparison of strain to capacitance directly. The files were synced using custom software developed within our group specifically for the Hioki LCR and Instron E3000 equipment. The gauge factor was then computed by Equation (2).

**Advanced Geometrical Model and Analytical Prediction for Capacitance and Gauge Factor:** Two methods for calculating geometries of the HACS was completed: 1) Simple calculation—initial to final state calculations based on the variables described in Section 2.1.3 (see Supporting Information for details). 2) Advanced calculation—the details of the full geometrical model can be found in the Supporting Information. This model calculated the exact geometrical solution of the twisted yarn at any strain under the following assumptions: i) The  $E_f$  and  $W_f$  were concentric and thus might be both modeled as helices in 3D sharing the same major axis. ii) The  $W_f$  geometry was independent of the  $E_f$ . Thus, the  $E_f$  geometry was entirely constrained by the  $W_f$ . iii) The  $E_f$  was locally stiff and did not comply to the wire, resulting in a line of contact traced out between the two fibres. iv) Capacitance could be estimated from the cross-section, integrated along the sensor (self-capacitance between coils was negligible). First,  $E_f$  and  $W_f$  were parameterized as helices in 3D space. At zero strain, the  $E_f$  was a helix with major radius zero and the  $W_f$  was a helix with major radius set so that it wrapped around the  $E_f$ . Some constraints were defined between the fibres (see Supporting Information for details) that described their major radii as a function of strain. The  $E_f$  length might be calculated from both its helical path and from Poisson's ratio, with both equations having dependence on the  $E_f$  diameter. This equality was solved numerically to obtain the 3D model. Both helices were sliced with a plane perpendicular to the main axis, yielding a set of closed curves defining the cross-section of the elastic, wire, and dielectric layers. With these curves, the cross-sections were analyzed with the arbitrary transmission line calculator software, ATLC2<sup>[21]</sup> to predict the resulting capacitance of the geometry. To analyze the GF versus engulfment, the position of the wires cross-section was manually shifted radially toward the center of the  $E_f$  by a fraction of its diameter. Engulfment here referred to  $W_f$  pushing into  $E_f$ , such that there was an increase in the contact area between the two fibers.

## Supporting Information

Supporting Information is available from the Wiley Online Library or from the author.

## Acknowledgements

The authors gratefully acknowledge ScopeM ETH Zurich for their support and assistance in this work, and Dr. Gisela Anna Kuhn from the Institute of Biomechanics ETH Zurich for running the X-ray  $\mu\text{CT}$ .

## Conflict of Interest

T.J.C., P.R., and C.M. are co-inventors on a patent that covers this technology (patent application EP22207284.5).

## Data Availability Statement

The data that support the findings of this study are available from the corresponding author upon reasonable request.

## Keywords

auxetics, capacitive sensors, fibers, helical auxetic yarn, metamaterials, strain sensor, textiles

Received: October 12, 2022

Revised: November 24, 2022

Published online: January 6, 2023

- 
- [1] Z. Jinyun, L. Yi, J. Lam, C. Xuyong, *Text. Res. J.* **2010**, *80*, 1965.
- [2] A. Ni Annaidh, K. Bruyere, M. Destrade, M. D. Gilchrist, M. Ottenio, *J. Mech. Behav. Biomed. Mater.* **2012**, *5*, 139.
- [3] H. M. A. Kolken, A. A. Zadpoor, *RSC Adv.* **2017**, *7*, 5111.
- [4] Y.-J. Lee, S.-M. Lim, S.-M. Yi, J.-H. Lee, S.-G. Kang, G.-M. Choi, H. N. Han, J.-Y. Sun, I.-S. Choi, Y.-C. Joo, *Extreme Mech. Lett.* **2019**, *31*, 100516.
- [5] J. Shintake, T. Nagai, K. Ogishima, *Front. Rob. AI* **2019**, *6*, 127.
- [6] R. Nur, N. Matsuhisa, Z. Jiang, M. O. G. Nayeem, T. Yokota, T. Someya, *Nano Lett.* **2018**, *18*, 5610.
- [7] H. Liu, M. Kollosche, J. Yan, E. M. Zellner, S. A. Bentil, I. V. Rivero, C. Wiersema, S. Laflamme, *Sensors* **2020**, *20*, 15.
- [8] R. Zeiser, T. Fellner, J. Wilde, *J. Sens. Sens. Syst.* **2014**, *3*, 77.
- [9] A. Atalay, V. Sanchez, O. Atalay, D. M. Vogt, F. Haufe, R. J. Wood, C. J. Walsh, *Adv. Mater. Technol.* **2017**, *2*, 1700136.
- [10] M. L. De Bellis, A. Bacigalupo, *Smart Mater. Struct.* **2017**, *26*, 085037.
- [11] Y. Jiang, Z. Liu, N. Matsuhisa, D. Qi, W. R. Leow, H. Yang, J. Yu, G. Chen, Y. Liu, C. Wan, Z. Liu, X. Chen, *Adv. Mater.* **2018**, *30*, 1706589.
- [12] J. Gu, J. Ahn, J. Jung, S. Cho, J. Choi, Y. Jeong, J. Park, S. Hwang, I. Cho, J. Ko, J.-H. Ha, Z.-J. Zhao, S. Jeon, S. Ryu, J.-H. Jeong, I. Park, *Nano Energy* **2021**, *89*, 106447.
- [13] P. B. Hook, K. E. Evans, J. P. Hannington, C. Hartmann-Thompson, T. R. Bunce, *US 8916262 B2*, **2014**.
- [14] M. R. Sloan, J. R. Wright, K. E. Evans, *Mech. Mater.* **2011**, *43*, 476.
- [15] R. Wu, S. Seo, L. Ma, J. Bae, T. Kim, *Nano-Micro Lett.* **2022**, *14*, 139.
- [16] W. Geng, T. J. Cuthbert, C. Menon, *ACS Appl. Polym. Mater.* **2021**, *3*, 122.
- [17] A. Frutiger, J. T. Muth, D. M. Vogt, Y. Mengüç, A. Campo, A. D. Valentine, C. J. Walsh, J. A. Lewis, *Adv. Mater.* **2015**, *27*, 2440.
- [18] H. Wang, Z. Liu, J. Ding, X. Lepró, S. Fang, N. Jiang, N. Yuan, R. Wang, Q. Yin, W. Lv, Z. Liu, M. Zhang, R. Ovalle-Robles, K. Inoue, S. Yin, R. H. Baughman, *Adv. Mater.* **2016**, *28*, 4998.
- [19] C. B. Cooper, K. Arutselvan, Y. Liu, D. Armstrong, Y. Lin, M. R. Khan, J. Genzer, M. D. Dickey, *Adv. Funct. Mater.* **2017**, *27*, 1605630.
- [20] C. Choi, J. M. Lee, S. H. Kim, S. J. Kim, J. Di, R. H. Baughman, *Nano Lett.* **2016**, *16*, 7677.
- [21] ATLC2 - Arbitrary transmission line calculator, <http://www.hdtvprimer.com/kq6qv/atlc2.html> (accessed: August 2022).